Hindawi
Advances in Materials Science and Engineering
Volume 2022, Article ID 7919532, 14 pages
https://doi.org/10.1155/2022/7919532

Research Article

Surface Flaw Detection of Plug Valve Material Using Infrared Thermography and Weighted Local Variation Pixel-Based Fuzzy Clustering Technique

V. Jacintha,[1] **S. Karthikeyan**,[2] **and P. Sivaprakasam**[3]

[1]*Department of Electronics & Communication Engineering, Sathyabama Institute of Science & Technology, Chennai 600119, India*
[2]*Department of Electronics & Communication Engineering, Sathyabama Institute of Science & Technology, Chennai, India*
[3]*Department of Mechanical Engineering, College of Electrical and Mechanical Engineering, Centre of Excellence-Nanotechnology, Addis Ababa Science and Technology University, Addis Ababa, Ethiopia*

Correspondence should be addressed to V. Jacintha; jacinthaece@gmail.com and P. Sivaprakasam; shiva@aastu.edu.et

Received 7 June 2022; Accepted 5 July 2022; Published 8 August 2022

Academic Editor: Vijayananth Kavimani

This study focuses on the identification and categorization of plug valve defects. We utilize a thermal fluke camera to obtain the plug valve thermal images. The thermal camera utilizes passive infrared thermography towards the identification of plug valve defects such as cracks, porosity, and internal defects. These flaws depict variation in surface temperature induced by heat flux. Infrared thermography is capable of identification of surface flaws such as cracks and subsurface flaws such as porosity. Its flaw identification range is effective only up to a certain depth in the metal. The heat flux variations are clearly visible for surface cracks and subsurface porosity. However, the heat flux shows no fluctuations for internal defects. Hence, to identify the internal defects in the metal, we opt for a combination of passive infrared thermography and dye penetrating test. In the dye penetrating test, a thinned paint is applied over the metal surface that aids in the identification of cracks, porosity, and internal defects as well. The PIT-DPT (passive infrared thermography-dye penetrating test) works in combination with weighted local variation pixel-based fuzzy clustering (WLVPBFC) to measure the depth of the defects. The defects were measured against parametric quantities such as F-value, precision, recall, accuracy, Jaccard index, TP, FP, TN, FN, FP rate, TP rate, and MCC. These parameters depict variations with regard to surface texture and extent of defect level. The PIT-DPT and WLVPBFC techniques identify metal flaws with 87.88% efficiency when evaluated against other existing algorithms.

1. Introduction

The plug valve utilized for defect evaluation is made of cast iron. Cast iron belongs to the family of iron-carbon alloys possessing carbon concentration of greater than 2%. The primary alloying substances of cast iron are carbon in the range of 1.8 to 4% and silicon in the range of 1 to 3%. Metal defects are obtained in times in the processing chain, while making the metal and yielding castings, during mechanical and pressure handling operations, because of thermal, chemical thermal, and electrochemical properties, and in tasks such as conjoining metals, storage, dispatch, and working. There are 3 major metal defects such as cracks, porosity, and internal defects that we are going to focus on. Several research works are carried out towards clustering diverse mathematical and data consisting of varied attributes. This is owing to its demand in real-time applications [1]. Cracks are surface or subsurface scissures that originate in a material. Cracks are caused due to utilizing hydrogen to weld ferrous metals, residuary stress, base metal contaminant, enhanced welding speed, reduced current, no preheating prior to welding, improper joint design, and huge amounts of sulphur and carbon in the metal. Cracks minimize the effectiveness of the weld by decreasing the weld dimension. They can develop and cause breakage of the entire metal part. There are a variety of cracks such as cooling, solidifying, centre crack, crater, abrasion, pickling, and heat treatment, machining ruptures, plating, fatigue,

creep, stress corrosion, and hydrogen cracks. Porosity is the occurrence of holes or voids in the weld. It happens due to freezing of gas expelled from the weld pool when it solidifies. The entrapped gas produces a hollow globule that gets feeble and can explode after certain duration. Porosity happens as an outcome of insufficient electrode oxidant, usage of longer arc, inappropriate gas cover, wrong surface treatment, usage of enhanced gas flow, polluted weld surface, presence of moisture, rust, paint, and oil. There are varied types of porosity: distributed porosity seems like fine pores. If they occur in huge quantities, they are termed as surface-breaking pores. If the pores are stretched, they are termed as wormholes. The existing NDT techniques enable the detection of pore flaws having a diameter of 0.13 mm and porosity flaws that are submerged at a depth of 1 mm [1]. In the final solidifying of the weld pool, we have crater pipe (gas porosity). Porosity will bring down the metal ductility and stiffness. Internal defects happen due to the following: welding current and welding speed are at their peak, use of faulty angle, heat distribution not uniform, diminution in fatigue strength, surface contaminants, misalignment, service failure, notch effect, hence preventing gas flow, porous and brittle weld joints, and material loss. The varied internal defects that happen in welds are undercut, incomplete fusion, incomplete penetration, slag inclusion, and spatter. The undercut is a furrow formed at the weld toe, scaling down the metal thickness. This ends up in a weak weld and workpiece. When the weld metal is not perfectly merged with the base metal, it results in incomplete fusion. When the weld metal does not completely go through the thickness of the joint, incomplete penetration takes place. When the solid covering material, flux thaws in the weld or weld surface, it causes slag inclusion to occur. Weld spatter comprises tiny particles of liquefied metal that are formed in proximity to the welding arc that binds to the gas shroud of the weld gun and thereby restricting gas flow.

Table 1 explains the novelty of the proposed technique.

(i) There are different types of nondestructive testing methods, among which we utilize dye penetrating test for identifying and categorizing metal defects. DPT is utilized for the detection of cracks and porosity.

(ii) To detect internal defects, we utilize passive infrared thermography. The testing of plug vales using DPT-PIT (dye penetrating test-passive infrared thermography) can be carried out on-site, on the very same premises of the plug valve.

(iii) In many instances, a combination of RGB and thermal imaging has enhanced the entire object detection process [2].

(iv) The experimentations are carried out on cast iron plug valves, showing effective outcomes to identify metal defects such as cracks, porosity, and internal defects.

2. Literature Survey

Srinivasan and Sadagopan studied the segmentation of the brain tissues during intensity nonuniformity and noise [4]. A similarity distance vector is used to estimate rough fuzzy regions based on both local spatial information and global spatial information. For weighted image estimation, the approach also uses a bounded support vector. The suggested algorithm's objective function is minimized for the segmentation of various brain tissues in MR images. Clustering algorithms for T1 and T2 MR images from the brain Web dataset are used to test the RFRBSFCM algorithm. Compared with other current state-of-the-art methods, the quantitative results show that the algorithm under consideration is more efficient. The fuzzy multi-characteristic clustering technique is based on fuzzy logic and clustering to achieve this objective. Fuzzy sets are utilized to express ambiguity in user query, similarity measure, and image content. Clustering is an unsupervised classification method that allows a tiny degree of control over clustering and dramatically enhances clustering performance. The preliminary results indicate that our suggested method is capable of attaining high precision and recall rates with improved computing efficiency [5]. Soft optimization techniques are used to detect liver cancer in abdominal liver imaging automatically. Performance is evaluated using entropy, energy, mean, standard deviation, accuracy, and elapsed time in this article. A novel automatic segmentation technique for detecting liver cancer is also being developed. Based on ROI and the adaptive watershed algorithm, a novel recommended technique is presented. Furthermore, the findings of this suggested study provide unambiguous information concerning normal and aberrant segmentation of the malignant region of the liver, allowing physicians to treat the problem in a consistent manner. To better segment tumours, region growth, intensity-based thresholding, and proposed statistical parameter-based segmentation approaches can be applied [6]. Fuzzy clustering enables effective segmentation even if the image to be processed is contaminated with noise [7]. To minimize the objective function, the algorithm requires an update on the membership function and cluster centres. Hence by linking the membership function, the number of iterations is reduced to a great extent. This procedure enables minimizing the objective function [8]. The key step in fuzzy clustering is selection of number of clusters and centroid initialization. Histogram smoothening automates this entire process. The number of peaks denotes the number of clusters. The gray level of each peak denotes the centroid of the cluster. Since this entire process is automated, it reduces the number of iterations and speeds up the procedure [9]. The segmentation of colour images is even more effective even in the presence of noise and requires a few number of iterations to complete the task [10]. Unsupervised learning is a procedure in which the data will not be labelled. The algorithm must automatically perform the clustering of data exclusively on its own. Here, fuzzy C-means clustering is an unsupervised learning procedure, which performs effectively except in the presence of noise. Hence to overcome this issue, the adaptive FCM algorithm is utilized that performs effectively even in the presence of noise [11]. The pixels in an image render sufficient details of the image. The image patch gives more information about the image, when compared to the pixels.

Table 1: Applicability and novelty of the proposed work.

Technique	Applicability	Remarks
Eddy current testing	Partially applicable	Detects subsurface flaws only up to 1 mm deep [1]
X-ray	Limited/not applicable	Flaws are not orthogonal to the radiation pattern. Operator at risk since exposed to radiation [1]
Ultrasonic inspection	Limited/ impossible	Lack of proper coupling between the probe and the material leads to severe echoing of signals and false alarms, thus misleading the inspection process [2]
Magnetic particle inspection	Not applicable	Inability to test nonferrous materials. Large currents are required that result in burning of the testing parts. Demagnetization is an issue [3]
Dye penetrant inspection	Applicable	Provides on-suite inspection. Lesser processing time with efficient results. Inexpensive in comparison with other NDT techniques

The image patch gives details about the image pixel and the cluster centre. Based on the distance of the image patch and the cluster centre, weights are assigned to each pixel in the image [12]. Kernel-based fuzzy clustering processes several features at the same time, thereby reducing the processing time [13]. The spatial or contextual data allow assigning labels to the pixels with the aid of the neighbouring pixels, thereby dealing with noise and other constraints [14]. The adaptive FCM possesses an adaptive factor that automatically changes the interval between the samples within every class and thereby extracts the features that belong to a particular sample. The greater the interval width between the samples, the more separable they are [15]. The spatial details are considered as a crucial attribute of the input image that needs to be classified. The spatial data of an image refer to the location of each and every pixel in the image. While getting to know the position of the pixel, the clustering is made happen more effectively [16]. Supervised FCM deals with the classification of defects utilizing labelled data, but unsupervised FCM refers to defect categorization when the data are not labelled. From the analysis, it is advisable to go for semi-supervised FCM in which part of the input data are labelled; utilizing this info, the algorithm is guided through the unsupervised areas of segmentation and classification [17]. FCM algorithm overcomes the effect of noise present in the image by assigning low membership values to those pixels that contain noise. Hence, those pixels containing noise get suppressed and do not enter the segmentation stage. The pixels that are noise-free are assigned with higher membership values, which further enter into the segmentation phase [18].

From the literature survey, the varied defects identify using various clustering algorithms. These other clustering algorithms are not adaptive to the local context, dependent on clustering parameters; hence, the clustering task becomes tedious. They need to update their contextual weight for each iteration. The objective is to propose a clustering algorithm that performs pixel-based fuzzy clustering using the weighted filter, in which the weights are automatically allocated to each pixel inside the local window, adaptive to the local context, independent of clustering parameters, thereby enabling the clustering task to be simplified with low computation cost.

3. Proposed System

There are various nondestructive testing (NDT) procedures utilized for the identification of defects in valves. Eddy current testing works on the principle of electromagnetic induction to identify flaws in the material under test. A current is passed through a coil adjacent to the test piece. Hence, the test piece starts generating Eddy currents that interfere with the current in the coil. As a result, a magnetic field is created in the coil. If a defect is present in the test piece, it causes variation in the Eddy current that in turn varies the amplitude and phase of the output signal. However, this technique can detect subsurface flaws submerged only up to 1 mm depth. Radiographic testing (RT) utilizes X-rays or gamma rays to evaluate the structure of the material under test towards detection of defects. However, the depth of penetration of X-rays is very low, capable to detect only surface flaws. This technique can also give misleading outcomes, in the presence of any dirt/foreign substances. Ultrasonic NDT testing utilizes sound waves for detecting defects in the test piece. The sound waves are generally high-frequency waves that traverse through a medium (piece of iron/steel) till they enter the border of another medium (air), at which instance gets reflected back. A detailed study of these reflections enables the evaluator to compute the test piece thickness and thereby detect surface and subsurface defects. If the surface of the specimen is not flat, it will create serious issues during probe coupling, which in turn results in echoes being generated. This will ultimately end up in erroneous measurements. Magnetic particle inspection (MPT) is a technique that involves magnetizing the material under test. Later magnetic substances are sprinkled over the surface of the test piece. If there is a defect in the test piece, the magnetic field gets disturbed, which causes magnetic flux leakage. Hence, the magnetic particles get grouped around the region of magnetic flux leakage, thereby indicating the defect. This technique is capable to detect only surface flaws and near subsurface flaws. Also, the specimen needs to be demagnetized at the end of the test, which becomes a time-consuming task.

In Figure 1, the three plug valve flaws, which are cracks, porosity, and internal defects, identify using the DPT-PIT method. This infrared method does not require an extraneous heat source.

The infrared emission radiated by the object is rather accumulating. Passive infrared thermography has the capability to render a temperature dispersion graph of the metal surface or joint throughout welding. Defective metal samples can induce unnatural temperature dispersion. If a particular area has an unnatural hot spot with respect to its

Figure 1: Block diagram of the proposed system.

surroundings, it points out to be a serious issue, where its temperature is in total variation with its surroundings. These data utilize to curb welding parameters to assure reliable joints, in materials. Infrared thermography (IRT) is a universally recognized condition-supervising tool where the temperature evaluates in a realistic noncontact fashion. Hence, there is no impairment to the metal test piece. It is applicable for defect detection in metal plug valves since the sizing and depth of defect can be identified by this method from one side by considering time evolution.

Dye penetrant inspection is a nondestructive testing method to detect flaws that are present in metals. The metal test piece is initially cleaned using SKC-S cleaner to get rid of dirt, paint, oil, grease, etc. If left uncleaned, it may lead to masking of defects and produce false results. The presence of dust/dirt/foreign substances may alter the thermal characteristics of the material and thereby result in erroneous NDT measurements [3]. The next step is application of penetrant, which is a bright coloured dye having high wetting capacity. The penetrant needs to douse into the flaws and requires a dwell time of 10–30 seconds. The following step is the removal of excess penetrant; if the excess penetrant is not removing properly, it may mask the defects and end up in false results during inspection, after which is the application of developer, which is available in aerosol spray tins that might employ acetone, isopropyl alcohol, or a mixed version of the two. The development time is generally 10 minutes to 120 minutes. There must be uniform coating of the developer, over the entire surface of the metal. The developer bleeds the penetrant out of the flaws onto the surface, to make it obviously visible. This process can figure out the location, orientation, and defect type. The dwell time is for the bloating action to occur.

3.1. Clustering. Clustering is the process of assigning the pixels of an image to clusters, in such a way that pixels in one cluster are alike, while pixels belonging to varied clusters are dissimilar. The objective is to form separate groups having similar attributes and allocate them into clusters. Clusters distinguish through similarity indices such as distance, connectivity, and intensity.

3.1.1. Fuzzy Clustering. Fuzzy clustering is a type of clustering in which each pixel can be a part of more than one cluster.

3.1.2. Fuzzy C-Means Clustering. Fuzzy c-means clustering algorithm was presented by Bezdek in 1981. It separates the image into clusters depending upon the distance of centre of cluster from the data points. It utilizes the Euclidean distance norm to separate the image into clusters. Normally, clustering algorithms are of four types: hierarchical, decomposing a

Step 1: Initialization of the window size, number of clusters, fuzzy membership matrix, and iteration counter.
Step 2: Initialization of centre of the cluster, for enhanced visualization of the segmented image; normally, cluster centre is in the range of cent = [0, 50,120,200].
Step 3: GRBF kernel
$K(x_i, v_j) = \exp(-\| x_i - v_j \|^2 / 2\sigma^2)$.
where "σ" denotes the kernel width.
Utilize maximum gray level as the kernel width. The kernel width of GRBF kernel is computed for improved accuracy.
Step 4: Computing "?" depending on the distance variances amidst all pixels:
$\sigma = [\sum_{i=1}^{N} (d_i - \overline{d})^2 / N - 1]^{1/2}$,
where $?_? = \|x_i - x'\|$ is the distance from the grayscale of pixel ? to the grayscale mean of all pixels and ? is the mean of all distances $?_?$.
Step 5: Computing the novel cluster centres
$v_j = \sum_{i=1}^{N} u_{ij}^m (K(x_i, v_j) x_i + \varphi_i K(\overline{x}_i, v_j)\overline{x}_i) / \sum_{i=1}^{N} u_{ij}^m (K(x_i, v_j) + \varphi_i K(\overline{x}_i, v_j))$.
Step 6: Computing the novel membership matrix
A membership function for a fuzzy set A on the universal set X is denoted as $\mu_A : X \to [0, 1]$, where every factor of X is mapped out to a value in the range of 0 and 1. Membership functions enable to render a pictorial representation of a fuzzy set.
$u_{ij} = ((1 - K(x_i, v_j)) + \varphi_i (1 - K(\overline{x}_i, v_j)))^{-1/(m-1)} / \sum_{k=1}^{c} (1 - K(x_i, v_k) + \varphi_i (1 - K(\overline{x}_i, v_k)))^{-1/(m-1)}$.

Step 7: Computing the objective function

$$J_{\text{ARKFCM}} = 2\left[\sum_{i=1}^{N}\sum_{j=1}^{c} u_{ij}^m (1 - K(x_i, v_j)) + \sum_{i=1}^{N}\sum_{j=1}^{c} \varphi_i u_{ij}^m (1 - K(\overline{x}_i, v_j))\right].$$

Step 8: Computing local average of each pixel, local variance of each pixel, local variation coefficient
$\text{LVC}_i = \sum_{k \in N_i} (x_k - \overline{x}_i)^2 / N_R * (\overline{x}_i)^2$,
where x_k is the grayscale of any pixel present in the local window N_i around the pixel I, N_R is the cardinality of N_i, and x_i' is its average grayscale.
Step 9: Computing local sum of LVC and exponential function
LVC is applied to an exponential function to deduce the weights inside the local window
$\zeta_i = \exp(\sum_{k \in N_i, i \neq k} \text{LVC}_k)$.
Step 10: Computing weight for each pixel. PixWgt: this function computes the weight for every pixel depending on the local variation coefficient
$\omega_i = \zeta_i / \sum_{k \in N_i} \zeta_k$.
The ultimate weight allotted to each pixel is related to mean grayscale of the local window

$$\varphi_i = \begin{cases} 2 + \omega_i, & \overline{x}_i < x_i \\ 2 - \omega_i, & \overline{x}_i > x_i \\ 0, & \overline{x}_i = x_i \end{cases}.$$

The parametric quantity ?? allots greater values for pixels having high LVC and lesser values for pixels with low LVC. When the local mean grayscale is the same as the central pixel grayscale, ?? is zero and the algorithm will function similarly to the standard FCM algorithm.
? can be substituted with the grayscale of the novel weighted image ?:
$\overline{\xi}_i = 1/2 + \max(\varphi_i)(x_i + 1 + \max(\varphi_i)/N_R - 1 \sum_{r \in N_i} x_r)$,
where x_r and N_i are the grayscale and neighbourhood of pixel i and N_R is the cardinality of N_i. The above formula ensures that the weighted image is free from parametric quantities that are difficult to adjust.
Step 11: Computing the final weights

Algorithm 1: Initializations.

density function, graph theoretic, and minimizing an objective function. The main concentration of this technique is on clustering by minimizing the objective function.

3.1.3. WLVPBFC. The weighted local variation pixel-based fuzzy clustering framework is proposed for the segmentation of plug valve defects. In the framework, the local average grayscale is substituted by grayscale of weighted filter, to obtain the contextual information. The standard Euclidean distance is substituted by the Gaussian radial basis function (GRBF) to obtain good accuracy. The regularization of parametric quantity will bring to increase segmentation robustness, conserve image particulars, and formulate a weighted image. The local variation coefficient is computed for each of the weighted image pixels. The primary advantages are adaptive to the local context, independency of clustering parameters, and reduced computational costs (Algorithm 1).

4. Results and Discussions

Figure 2 depicts the clustering results of a plug valve obtained using a median filter. The median filter is a nonlinear

Figure 2: ARKFCM outputs using the median filter for defective and healthy thermal images.

digital filtering method and is commonly utilized to get rid of noise present in an image.

The median filter substitutes a pixel by the median, of all pixels in the neighbouring window. Since the median must generally be the value of one of the pixels in the neighbouring window, the median filter does not produce novel impractical pixel values when the filter extends over an edge. Hence, the performance of the median filter is enhanced in maintaining incisive edges. One of the primary issues with the median filter is that it is relatively costly and complicated to calculate.

$$y[m,n] = \text{median}\{x[i,j], (i,j) \in w\}. \quad (1)$$

The defective plug valve thermal images are shown to contain defects such as cracks, porosity, and internal defects. The process is repeated from one iteration to the next by varying the window size (WS) and the cluster number (CN). The defective plug valve thermal images having WS = 1 and CN = 2 show cracks; WS = 5 and CN = 3 shows porosity defects; and WS = 21 and CN = 15 shows internal defects. However, the default window size (size of the local window) is 3. The clustering results of healthy plug valve thermal images do not contain any of the abovementioned defects. This clustering process enables to detect the plug valve defects in a more efficient manner but requires updating their contextual weights for every iteration, which is the primary cause of their greater computational cost.

Figure 3 shows the clustering results of plug valve that are obtained using the average filter. The average filter performs by passing across the image pixel by pixel, substituting every value with the mean value of the pixels in the neighbourhood, considering itself.

Even if one of the pixels has an untypical value, it can drastically disturb the mean value of all the neighbouring pixels. When the filter spans across an edge, the filter will extrapolate novel values for edge pixels, resulting in blurred edges. This becomes an issue if sharp edges are expected in the output.

The defective plug valve thermal images are shown to contain defects such as cracks, porosity, and internal defects. The process is repeated from one iteration to the next by varying the window size (WS) and the cluster number (CN). The defective plug valve thermal images having WS = 3 and CN = 2 shows cracks; WS = 7 and CN = 4 shows porosity defects; and WS = 15 and CN = 8 shows internal defects. However, the default window size (size of the local window) is 3. The clustering results of healthy plug valve thermal images do not contain any of the abovementioned defects. This clustering process enables to detect the plug valve defects in a more efficient manner but require updating their contextual weights for each iteration, which is the primary cause of their greater computational cost. The above drawback can be overcome using the weighted filter.

Figure 4 shows the clustering outputs of healthy and defective plug valve thermal images, obtained using the weighted filter.

The type of clustering used is weighted local variation pixel-based fuzzy clustering. In this technique, we compute the weight for every pixel depending on the local variation coefficient. Initially, the local average/mean of every pixel is computed. Then, the local variance of each pixel is computed. Using this, the local variation coefficient (LVC) is determined. Further, the summation of the LVC is

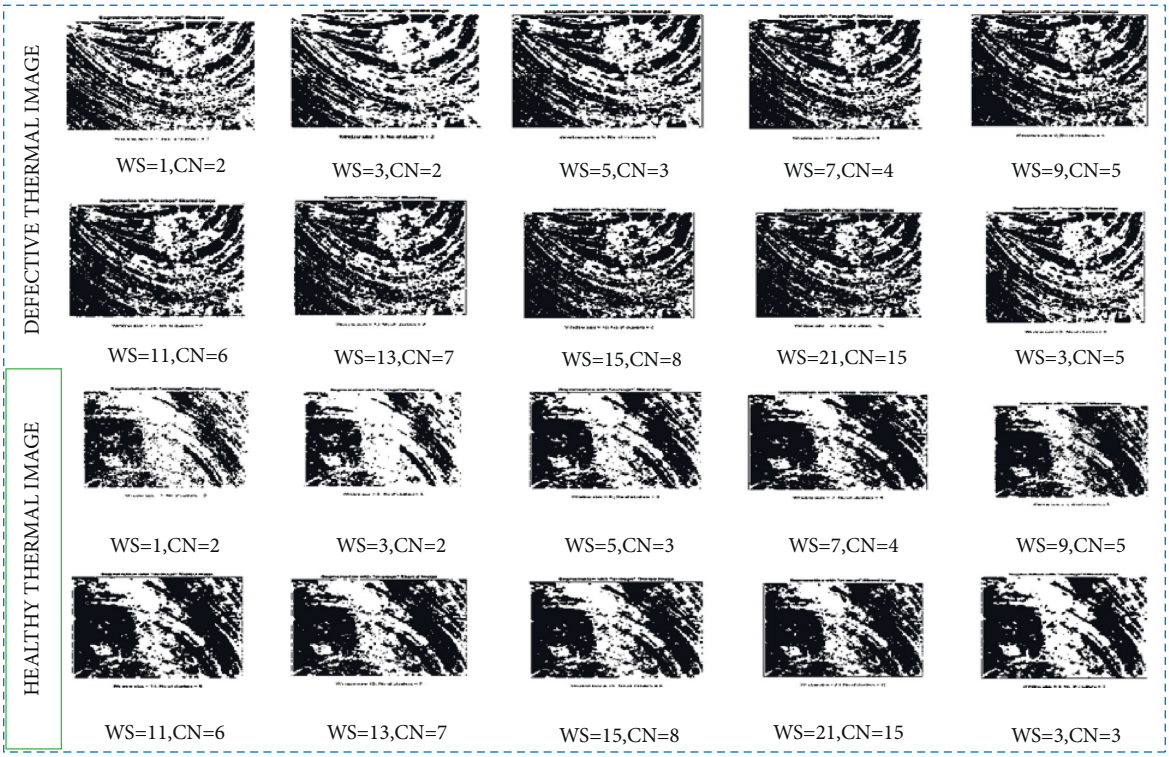

Figure 3: ARKFCM outputs using the average filter for defective and healthy thermal images.

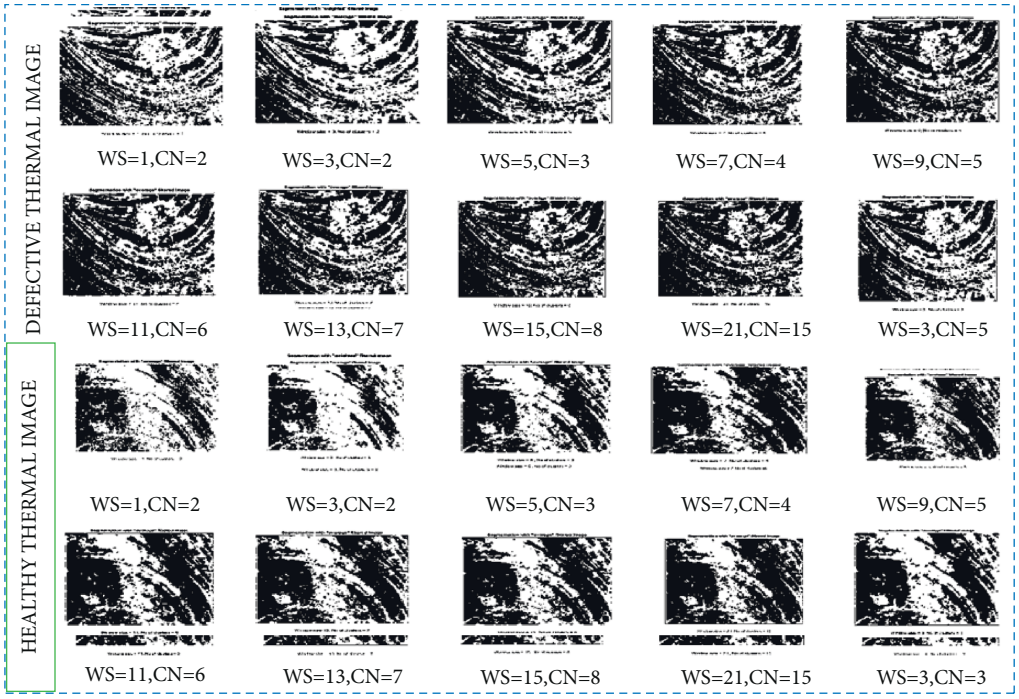

Figure 4: ARKFCM outputs using the weighted filter for defective and healthy thermal images.

computed. Finally, we apply this summation to an exponential function, to determine the weights of the pixel inside a local window. At last, we compute the weight for every individual pixel. The pixel that seems to be brighter when compared to the mean grayscale of its neighbouring pixels will possess a higher LVC value, and hence, greater weight is allotted to that pixel. Similarly, the pixel that seems to be less bright when compared to the mean grayscale of its neighbouring pixels will possess a lower LVC value, and hence, lesser weight is allotted to that pixel. When the local mean

grayscale equals the central pixel grayscale, the weight allotted to that pixel is zero. However, in this manner weights are allotted to every pixel inside the local widow. This allocation of weights simplifies the clustering task, and hence, segmentation is performed much effectively and easily, with less computational cost and at a much faster manner. Other FCM algorithms require updating their contextual weights for each iteration, which is the primary cause of their greater computational cost and time consumption.

Table 2 shows the various evaluation parameters that are considered to prove that the weighted filter is very efficient when compared with the median and average filters.

4.1. True Positive, True Negative, False Positive, and False Negative. A true positive is a result where the framework accurately anticipates the positive category. Likewise, a true negative is a result where the framework perfectly anticipates the negative category. A false positive is a result where the framework fallaciously anticipates the positive category. False negative is a result where the framework wrongly anticipates the negative category.

4.2. Accuracy. Accuracy is the ratio of correct anticipations (both true positives and true negatives) among the entire instances studied.

$$\text{Accuracy} = \frac{(\text{TP} + \text{TN})}{(\text{TP} + \text{TN} + \text{FP} + \text{FN})}. \tag{2}$$

4.3. Precision and Recall. Precision (also termed as positive predictive value) is the ratio of relevant cases to the retrieved cases, while recall (alias sensitivity) is the ratio of the total number of relevant cases actually retrieved.

$$\begin{aligned} \text{Precision} &= \frac{\text{TP}}{(\text{TP} + \text{FP})} \\ \text{Recall} &= \frac{\text{TP}}{\text{P}} \\ \text{P} &= \text{TP} + \text{FN} \\ \text{N} &= \text{FP} + \text{TN} \\ \text{FP rate} &= \frac{\text{FP}}{\text{N}} \\ \text{TP rate} &= \frac{\text{TP}}{\text{P}}. \end{aligned} \tag{3}$$

4.4. F-Measure. The F_{value} (F-score or F-measure) is a valuation metric for a test's exactitude. A standard that merges precision and recall is the harmonic mean of precision and recall, the conventional F-measure, or balanced F-score:

$$\text{Fvalue} = 2 * \frac{((\text{precision} * \text{recall})}{(\text{precision} + \text{recall}))}. \tag{4}$$

Table 2: Evaluation metrics.

S. no	Evaluation standards	Adaptive regularized kernel-based FCM		
		Weighted filter	Average filter	Median filter
		Window size 3 cluster number 2		
1	Accuracy	0.6944	0.6878	0.6800
2	FN	3637	3010	3831
3	FP	3239	3790	3368
4	F prate	0.6207	0.6289	0.6087
5	F value	0.7987	0.7984	0.78i9
6	Jaccard index	0.6649	0.6644	0.6430
7	MCC	0.1646	0.1572	0.1612
8	Precision	0.8082	0.7803	0.7959
9	Recall	0.7895	0.8173	0.7742
10	TN	1979	2236	2165
11	TP	13645	13464	13136
12	T prate	0.7895	0.8173	0.7742

This standard is roughly the mean of precision and recall and is normally the harmonic mean, which, for the context of two numbers, co-occurs with the square of the geometric average fractioned by the arithmetic average. F-measure is perfect when its value equals unity.

4.5. Jaccard Index. When comparing finite sample sets, the Jaccard coefficient measures similarity, and is defined as the size of the intersection fractioned by the size of the union of the sample sets:

$$J(A, B) = \frac{|A \cap B|}{A \cup B} = \frac{A \cap B}{|A| + |B| - |A \cap B|}. \tag{5}$$

4.5.1. MCC. The MCC is a correlation coefficient between the observed and anticipated binary classifications; it generates a value between −1 and + 1. A coefficient of +1 denotes a perfect anticipation, 0 denotes no better than stochastic anticipation, and −1 denotes total discrepancy between anticipation and observation. The coefficient considers true and false positives and negatives and is normally looked upon as a balanced measure that can be utilized even if the categories are of extremely varied sizes.

$$\text{MCC} = \frac{(\text{TP} * \text{TN} - \text{FP} * \text{FN})}{\sqrt{((\text{TP}+\text{FP}) * (\text{TP}+\text{FN}) * (\text{TN}+\text{FP}) * (\text{TN}+\text{FN}))}}. \tag{6}$$

5. Output Graphs

5.1. Neural Network Training Model. The neural network training model lists the following parameters. Epoch is the time taken to complete one full cycle in training the total number of samples in the neural network. It takes into account one forward pass and one backward pass. Iterations are the total number of passes required to train the samples. Time denotes the duration taken to train each sample. Performance indicates the efficiency of each of the three different types of images. Gradient represents the percentage

Table 3: Iteration parameters.

S. no	Parameters	Bad-bad image	Good-bad image	Good-good image
1	Epoch	11 iterations	25 iterations	14 iterations
2	Time	3 sec	5 sec	0 sec
3	Performance	0.546	0.56	0.599
4	Gradient	0.00729	0.0121	0.00875
5	Validation checks	6	6	6

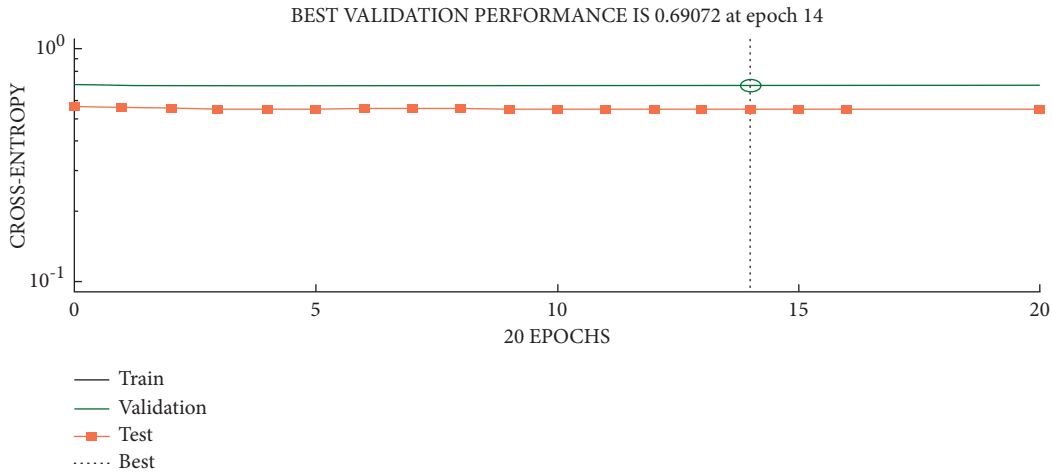

Figure 5: Performance plot.

amount of deviation that exists between the original input image and the output image. Validation checks indicate the number of times the verification has taken place. Table 3 shows the various iteration parameters utilized to evaluate the performance of the proposed technique.

5.1.1. Performance Plot. The performance plot shown in Figure 5 is the plot between the number of epochs on the *X*-axis and the cross-entropy values on the *Y*-axis. Epoch is the time taken to complete one full cycle. Cross-entropy evaluates the deviation amidst three probability distributions (training, validation, and testing) for a particular random variable or set of events. There are four lines, train, validation, test, and best. To affirm that training is performing effectively, the other three lines must lie on the best (dotted) line or in close proximity to it. If any of the three (training, validation, and testing) lines converge or pass beside the best (dotted) line, it reveals that convergence is taken place; else, the network is to be trained again. The training dataset is utilize to cultivate the candidate algorithms, and the validation dataset is utilized to analyze their operations and determine which one to choose and the test dataset is utilized to fetch the evaluation metrics such as accuracy, sensitivity, specificity, and F-measure. This plot enables us to determine the best fit among training, validation, and testing and also at what instance it occurs. In the case of defective-defective image, the best fit occurs at epoch 4 having a value equal to 0.5993. In the case of healthy-defective image, the best fit occurs at epoch 19 having a value equal to 0.53649. In the case of healthy-healthy image, the best fit occurs at epoch 8 having a value equal to 0.50936.

5.1.2. Training State. The training state graph shown in Figure 6 denotes the present advancement/training status at a particular instant while training is ongoing. In this case, six-validation errors are observed, and it denotes that when six-validation check faults are generated at the same time, then training will terminate. A validation check error is generated when the dataset has a few issues, such as certain instances that are not apprehensible by the training algorithm. The first training state graph is a plot between number of epochs on the *X*-axis and the gradient on the *Y*-axis. The gradient shows the amount of deviation of the healthy-defective image from the healthy-healthy image. For defective-defective image, initially at 0 epoch, the gradient had a higher value, which gradually decreases, and at epoch 11, the gradient has a least value equal to 0.0011818, which is approximately equal to zero. Hence, having a gradient value to be equal to zero indicates that there is not much deviation between the two images. For healthy-defective image, initially at 0 epoch, the gradient had a higher value, which gradually decreases, and at epoch 25, the gradient has a least value equal to 0.00064096, which is approximately equal to 0. For healthy-healthy image, initially at 0 epoch the gradient had a higher value, which gradually decreases, and at epoch 14, the gradient has a least value equal to 0.0028701, which is approximately equal to zero.

5.1.3. Error Histogram. Error histogram shown in Figure 7 is the graph of the errors between target values and anticipated values after a feed-forward neural network is trained. There are completely 20 bins. Bins denote the count of vertical bars observed on the histogram. The zero error line represents the

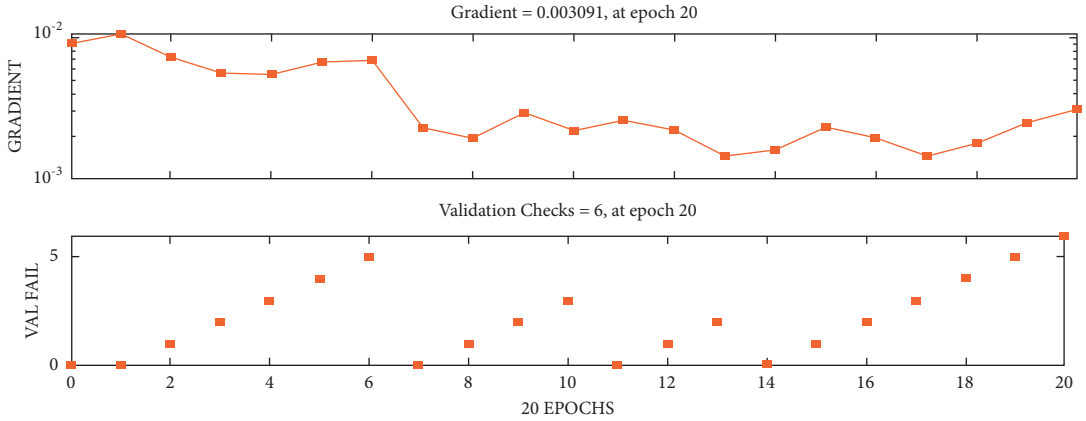

Figure 6: Training state for healthy-healthy image.

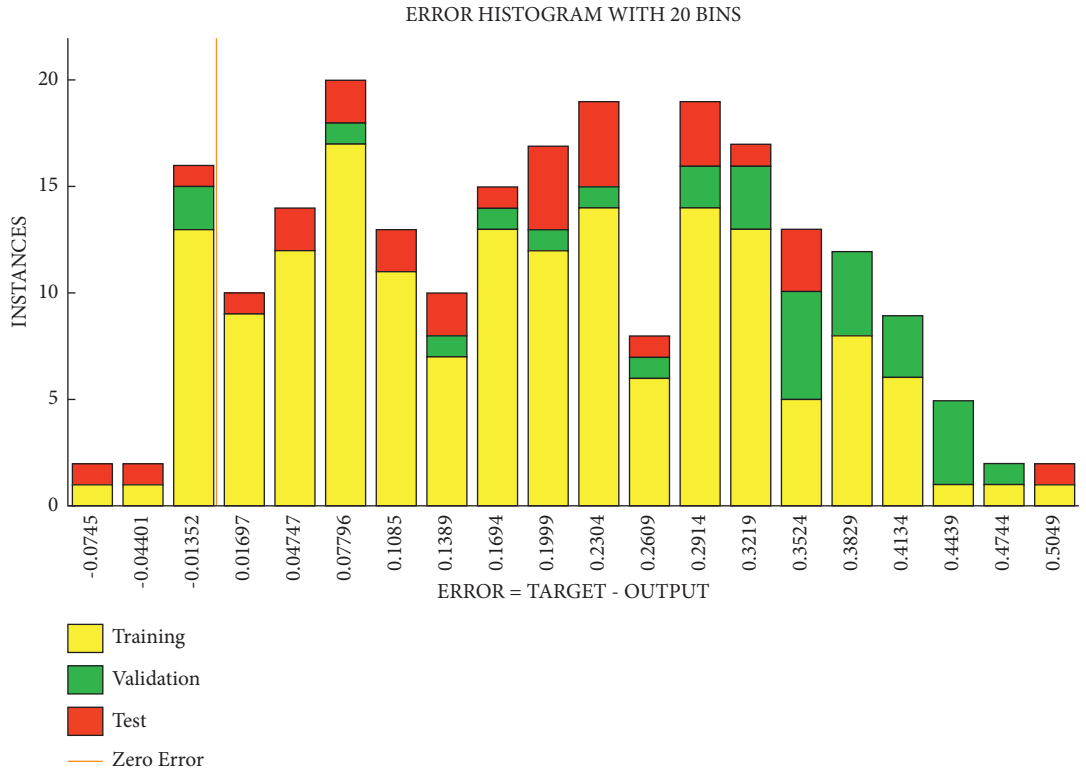

Figure 7: Error histogram for healthy-healthy image.

zero error value on the error axis (i.e., *X*-axis). For defective-defective image, the aggregate neural network error is in the range of -0.1318 to 0.4742. This range is fractioned into 20 bins, so that the width of every bin is (0.4742-(−0.1318))/20 = 0.0303. Every vertical bar denotes the count of the dataset samples that belongs to specific bin. For instance, in the middle of the histogram, there exists a bin representing the error of -0.00418 and the height of that bin for the validation dataset is 16. It implies that 16 samples from the validation dataset have an error lying in that range. Likewise, for healthy-defective image, the smallest amount of error 0.003858 roughly equals 0 and the height of that bin for the validation dataset is 16. For healthy-healthy image, the smallest amount of error -0.0099 roughly equals zero and the height of that bin for the validation dataset is 17.

5.1.4. Confusion Matrix. A confusion matrix (or error matrix) is generally utilized as a quantifiable technique for characterizing image classification precision. It brings out the parallelism between the classification output and the image taken as reference. A confusion matrix is an nxn matrix in which every row depicts the real classification of a particular data and every column depicts the anticipated classification. The precision of an image can be checked by viewing the diagonal cells of the confusion matrix, which

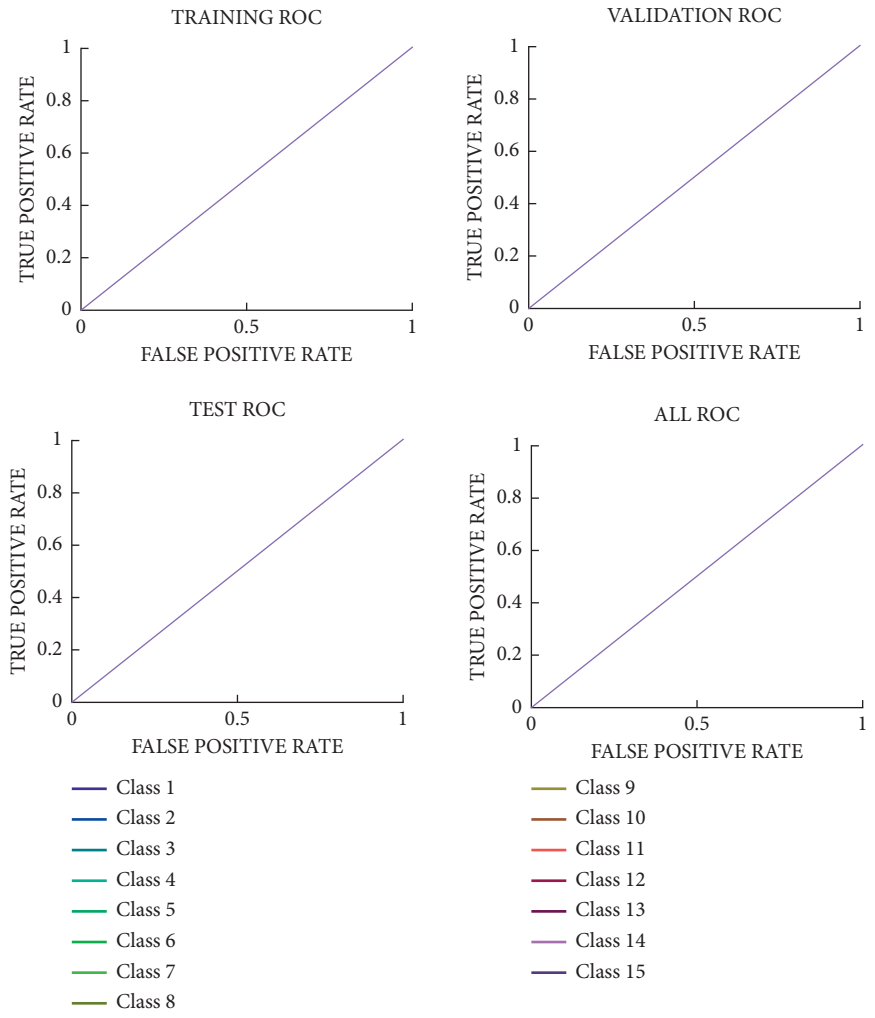

Figure 8: Receiver output characteristics graph for healthy-healthy image.

indicate the count of the perfect classifications. A healthy image will have greater values along the diagonal and lesser values in the cells apart from the diagonal. In addition, one can determine whether the model is not performing well, by evaluating the greater values on the non-diagonal cells in the matrix. If so, these cells comprise classification errors, i.e., instances in which there exists no correspondence between the reference image and classified image. However, these evaluations can be utilized to detect instances in which the precision is great, but the prototype is continuously performing the wrong classification of similar information.

5.2. Receiver Output Characteristic Graph. A receiver operating characteristic curve shown in Figure 8, or ROC curve, is a graphical representation that exemplifies the efficiency of a binary classification model as its discriminating threshold is altered. Classification accuracy is the total number of perfect classifications. The ROC curve is generated by plotting the true-positive rate (TPR) versus the false-positive rate (FPR) at varying threshold levels. ROC analysis renders tools to choose optimum models and cast aside suboptimal models. Bringing down the threshold level

25	54	12	23	31
41	32	42	64	25
24	46	50	55	65
49	53	56	61	60
57	61	66	71	76

Figure 9: Matrix to compute magnitude and orientation.

classifies many pixels as positive, thereby enhancing both false positives and true positives. Hence, the ROC curve can be utilized to choose a threshold for a classification model that enhances the true positives and reduces the false positives. The ROC curves for the training state, validation state, and test state are obtained individually. Then, a combined version of all the states and the final ROC curve are obtained.

5.2.1. SIFT. An image-matching algorithm recognizes the primal characteristics from an image and is capable of matching these characteristics to a novel image of the similar object. SIFT aids in locating these primal features generally

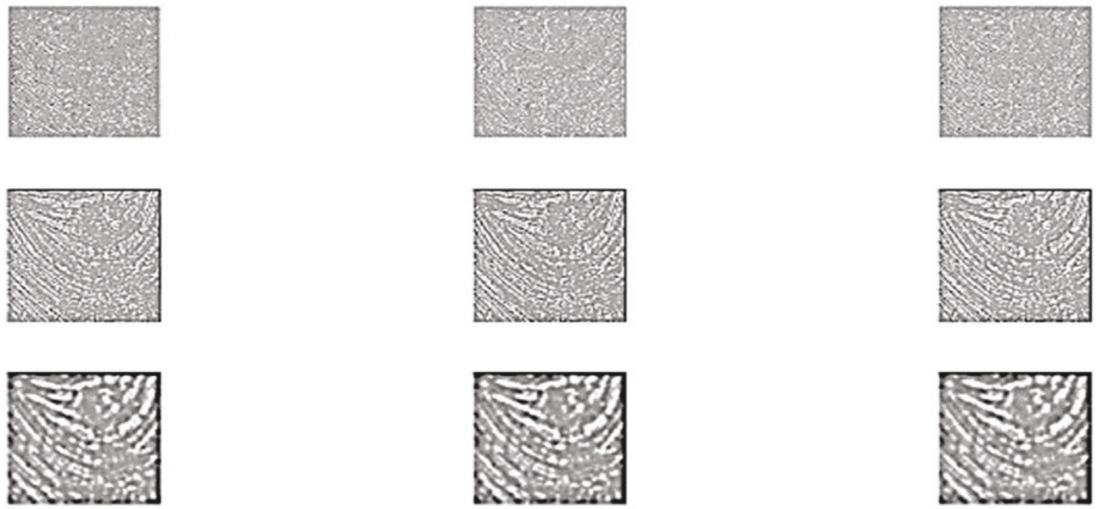

Figure 10: Output graph showing key points that do not match.

Figure 11: Output graph showing key points that perfectly match.

termed as "key points" of the plug valve image. These key points must be robust in such a way that, even if there is any variation in the scale, rotation, or angle of the image, key points are utilized for varied computer vision applications, such as image matching and object identification. The next phase is the construction of the scale space. Scale space is a grouping of several plug valve image possessing varied scales, which are obtained from an individual plug valve thermal image. This is performed to identify the unique features that show no variation in all the images whose scale has been varying. Difference-in-Gaussian function is utilized to remove or lessen image noise. Post-utilizing Gaussian blurs the texture, and less vital particulars are withdrawn from the image and only applicable data such as shape and edges are retained. The difference in Gaussian is a feature enhancement algorithm that deals with subtracting the blurred version of an original image from a less blurred version of the same image. Hence, we have confidently enhanced the vital features. Key point localization (selection) determines the primal key points from the image that can be utilized for feature matching. The aim is to determine the local maxima and minima for the images. It is performed by equating each image pixel with its adjacent pixels. This enables to get rid of low contrast key points, those that lie in close proximity to the edge, not sturdy to noise. Next is to specify an orientation to every key point so that their alignment does not vary, even if the image is rotated or slightly changed in angle. The magnitude and orientation are computed using the matrix shown in Figure 9.

To determine the magnitude and orientation for the central pixel highlighted in yellow, for this, initially the gradients in x and y directions are computed by fetching the difference between 55 and 46 and 56 and 42. The gradient values are $G_X = 9$ and $G_Y = 14$, respectively.

$$\text{Magnitude} = \sqrt{((G_X)^2+(G_Y)^2)} = 16.64$$

$$\Phi = \tan(G_Y/G_X) = \tan(1.55) = 57.17$$

The magnitude denotes the pixel intensity, and the orientation gives the pixel direction.

5.2.2. Histogram for Magnitude and Orientation. The bins for the angle values, such as 0–9, 10–19, 20–29, till 360, are plotted on the X-axis. In our case, the angle value is 57, and

hence, it will lie in the 6^{th} bin. The 6^{th} bin value will be proportional to the pixel magnitude, 16.64. This computation is performed for all the pixels surrounding the key point. At one particular instance, the graph would elevate to its maximum level. The bin at which we view this elevation is considered to be the key point orientation. In addition, if there exists a second elevation (viewed between 80 and 100%), then another key point is yielded. In this manner, the number of key points is increased. We utilize the neighbouring pixels, their magnitude, and orientation, to create a distinct fingerprint for this key point termed a "descriptor." In the given outputs, the gray images shown in Figure 10 denote those in which the key points do not match. The blue and green outputs shown in Figure 11 denote those in which the key points match perfectly.

6. Conclusions

This research work is based on weighted local variation pixel-based fuzzy clustering (WLVPBFC), in which the clustering task becomes easy by allocating/calculating the weights of each pixel. This is performed by computing the local variation coefficient. This enables the segmentation to be carried out more effectively, easily, faster, and with lesser computational cost. The clustering results of normal FCM using average filter and median filter are utilized for comparison purpose. It is determined that the FCM using average and median filter requires updating their contextual information for each iteration, which results in greater computational cost and time consumption. The WLVPBFC using weighted filter for plug valve thermal images outperforms the normal FCM using average filter and median filter in terms of accuracy of 69.44%, precision of 80.82%, Jaccard index of 0.6649, and MCC of 0.1646. The evaluation graphs show that the best results are obtained for healthy-healthy plug valve thermal images. In addition, using SIFTS the matching features/key points are obtained with a magnitude of 16.64 and phase value of 57.17. In future, this concept can be applied using deep learning algorithms.

Data Availability

The data used to support the findings of this study are included within the article.

Conflicts of Interest

The authors declare that they have no conflicts of interest regarding the publication.

References

[1] M. Machado, L. F. S. G. Rosado, N. A. M. Mendes, R. M. M. Miranda, and d. J. G. Santos, "New directions for inline inspection of automobile laser welds using non-destructive testing," *International Journal of Advanced Manufacturing Technology*, vol. 118, no. 3-4, pp. 1183–1195, 2022, Page No :1183–1195.

[2] S. B. Kera, A. Tadepalli, and J. J. Ranjani, *A Paced Multi-Stage Block-wise Approach for Object Detection in thermal Images*, The Visual Computer, 2022.

[3] R. Shrestha, S. Sfarra, S. Ridolfi, G. Gargiulo, and W. Kim, "A numerical–thermal–thermographic NDT evaluation of an ancient marquetry integrated with X-ray and XRF surveys," *Journal of Thermal Analysis and Calorimetry*, vol. 147, no. 3, pp. 2265–2279, 2021.

[4] A. Srinivasan and S. Sadagopan, "Retracted article: rough fuzzy region based bounded support fuzzy C-means clustering for brain MR image segmentation," *Journal of Ambient Intelligence and Humanized Computing*, vol. 12, no. 3, pp. 3775–3788, 2021.

[5] P. K. Kavitha and V. P. Saraswathi, "Retracted article: content based satellite image retrieval system using fuzzy clustering," *Journal of Ambient Intelligence and Humanized Computing*, vol. 12, no. 5, pp. 5541–5552, 2021.

[6] V. Hemalatha and C. Sundar, "Retracted article: automatic liver cancer detection in abdominal liver images using soft optimization techniques," *Journal of Ambient Intelligence and Humanized Computing*, vol. 12, no. 5, pp. 4765–4774, 2021.

[7] J. Miao, X. Zhou, and T. Z. Huang, "Local segmentation of images using an improved fuzzy C-means clustering algorithm based on self-adaptive dictionary learning," *Applied Soft Computing*, vol. 91, p. 106200, 2020.

[8] Q. Wang, X. Wang, C. Fang, and W. Yang, "Robust fuzzy c-means clustering algorithm with adaptive spatial & intensity constraint and membership linking for noise image segmentation," *Applied Soft Computing*, vol. 92, Article ID 106318, 2020.

[9] P. Valsalan, P. Sriramakrishnan, S. Sridhar et al., "Knowledge based fuzzy c - means method for rapid brain tissues segmentation of magnetic resonance imaging scans with CUDA enabled GPU machine," *Journal of Ambient Intelligence and Humanized Computing*, Article ID 0123456789, 2020.

[10] V. M. Dante, J. M. V. Kinani, and J. d. J. Rubio, "Color-based image segmentation by means of a robust intuitionistic fuzzy C-means algorithm," *International Journal of Fuzzy Systems*, vol. 22, no. 3, pp. 901–916, 2020.

[11] Y. Gao, D. Wang, J. Pan, Z. Wang, and B. Chen, "A novel fuzzy c-means clustering algorithm using adaptive norm," *International Journal of Fuzzy Systems*, vol. 21, no. 8, pp. 2632–2649, 2019.

[12] Y. Tang, F. Ren, and W. Pedrycz, "Fuzzy C-Means clustering through SSIM and patch for image segentation," *Applied Soft Computing J.*, p. 2019, 105928.

[13] P. Das and A. Das, "A fast and automated segmentation method for detection of masses using folded kernel based fuzzy c-means clustering algorithm," *Applied Soft Computing*, vol. 85, Article ID 105775, 2019.

[14] A. Halder and N. Talukdar, "Robust brain magnetic resonance image segmentation using modified rough-fuzzy C-means with spatial constraints," *Applied Soft Computing*, vol. 85, Article ID 105758, 2019.

[15] G. Feng, M. Ni, S. Ou, W. Y, and J. Xu, "A Preferential Interval-Valued Fuzzy C-means algorithm for remotely sensed imagery classification," *International Journal of Fuzzy Systems*, vol. 21, no. 7, pp. 2212–2222, 2019.

[16] G. Feng, M. Ni, S. Ou, and W. Yan, "Means algorithm for remotely sensed imagery classification," *International Journal of Fuzzy Systems*, 2019.

[17] C. Wan, X. Yuan, X. Dai, T. Zhang, and Q. He, "A self-adaptive multi-objective harmony search based fuzzy clustering technique for image segmentation," *Journal of Ambient Intelligence and Humanized Computing*, vol. 1-16, 2018 [14].

[18] P. Kaur, "Intuitionistic fuzzy sets based credibilistic fuzzy C-means clustering for medical image segmentation," *International Journal of Information Technology*, vol. 9, no. 4, pp. 345–351, 2017.